














A hidden active galactic nucleus population: the first radio luminosity functions constructed by physical process

Leah K. Morabito ^{1,2}★, R. Kondapally ³, P. N. Best ³, B.-H. Yue ³, J. M. G. H. J. de Jong ⁴,
F. Sweijen ¹, Marco Bondi ⁵, Dominik J. Schwarz ⁶, D. J. B. Smith ⁷, R. J. van Weeren ⁴, H. J.
A. Röttgering ⁴, T. W. Shimwell ^{4,8} and Isabella Prandoni ⁵

¹Centre for Extragalactic Astronomy, Department of Physics, Durham University, Durham DH1 3LE, UK

²Institute for Computational Cosmology, Department of Physics, Durham University, South Road, Durham DH1 3LE, UK

³Institute for Astronomy, University of Edinburgh Royal Observatory, Blackford Hill, Edinburgh EH9 3HJ, UK

⁴Leiden Observatory, Leiden University, PO Box 9513, NL-2300 RA Leiden, the Netherlands

⁵INAF – Istituto di Radioastronomia, Via Gobetti 101, I-40129 Bologna, Italy

⁶Fakultät für Physik, Universität Bielefeld, Postfach 100131, D-33501 Bielefeld, Germany

⁷Centre for Astrophysics Research, University of Hertfordshire, College Lane, Hatfield AL10 9AB, UK

⁸ASTRON, Netherlands Institute for Radio Astronomy, Oude Hoogeveensedijk 4, NL-7991 PD Dwingeloo, the Netherlands

Accepted 2024 November 5. Received 2024 November 5; in original form 2024 October 8

ABSTRACT

Both star formation (SF) and active galactic nuclei (AGNs) play an important role in galaxy evolution. Statistically quantifying their relative importance can be done using radio luminosity functions (RLFs). Until now these relied on galaxy classifications, where sources with a mixture of radio emission from SF and AGN are labelled as either a star-forming galaxy or an AGN. This can cause the misestimation of the relevance of AGN. Brightness temperature measurements at 144 MHz with the International LOw Frequency ARray telescope can separate radio emission from AGN and SF. We use the combination of sub-arcsec and arcsec resolution imaging of 7497 sources in the Lockman Hole and ELAIS-N1 fields to identify AGN components in the sub-arcsec resolution images and subtract them from the total flux density, leaving flux density from SF only. We construct, for the first time, RLFs by physical process, either SF or AGN activity, revealing a hidden AGN population at $L_{144\text{ MHz}} < 10^{24}\text{ W Hz}^{-1}$. This population is 1.56 ± 0.06 more than expected for $0.5 < z < 2.0$ when comparing to RLFs by galaxy classification. The star-forming population has only 0.90 ± 0.02 of the expected SF. These ‘hidden’ AGNs can have significant implications for the cosmic SF rate and kinetic luminosity densities.

Key words: galaxies: active – galaxies: evolution – galaxies: star formation – radio continuum: galaxies.

1 INTRODUCTION

The extent to which active galactic nuclei (AGNs) impact galaxy formation is a major open question in astrophysics. It is clear that there is an influence, from both observational and theoretical standpoints. Observations have revealed tight scaling relations between the mass of a supermassive black hole and its host galaxy (see e.g. Kormendy & Ho 2013, and references therein), while cosmological simulations require some form of AGN feedback (Bower et al. 2006; Croton et al. 2006) to be able to reproduce the observed galaxy population. The cosmic histories of AGN activity and star formation (SF), and by extension the interplay between them, are interlinked. It is necessary to quantify the contribution of each process to understand the importance of either or both of them. Relying on overall galaxy classification can overestimate or underestimate the contributions of each process; for example, by considering all of the radio emission in a galaxy classified as ‘star-forming’ to be due to SF, when some

may be due to AGN. Quantifying these contributions is the goal of this letter.

Decomposing AGN activity from SF on a per-galaxy basis is a difficult problem at any wavelength. Efforts have been made to do this via mid-infrared spectral decomposition using template fitting (e.g. Laurent et al. 2000; Hernán-Caballero et al. 2015; Li et al. 2024). Multiwavelength approaches use spectral energy distribution (SED) fitting, which uses information from as many observed bands as possible to jointly fit galaxy and AGN components (e.g. Calistro Rivera et al. 2016; Boquien et al. 2019; Pacifici et al. 2023). However, SED fitting is costly as it relies on observations from a variety of instruments, which then have to be carefully cross-matched, and there can be degeneracy in the fits. Varying selection effects across the different bands can also present a problem.

An alternative method to unambiguously identify the AGN component(s) in a galaxy is through brightness temperature, T_b , measurements in the radio waveband. Observations of radio emission have the advantage of being unobscured by dust or gas, so there are minimal observational biases. Models of radio emission from SF predict an upper limit to the surface brightness that can be produced, even in starburst galaxies (Condon 1992). Surface brightness that

* E-mail: leah.k.morabito@durham.ac.uk

is detected above this limit therefore has to be attributed to AGN activity. Brightness temperature is inversely proportional to frequency, ν , and resolution, θ : $T_b \propto \nu^{-2}\theta^{-2}$. Traditionally brightness temperature measurements require very long baseline interferometry (VLBI), which reach milliarcsec resolutions at GHz frequencies (e.g. Middelberg et al. 2013; Herrera Ruiz et al. 2017; Radcliffe et al. 2018) to achieve enough T_b sensitivity to make meaningful measurements. In Morabito et al. (2022a, hereafter M22), we demonstrated that this can be done using sub-arcsecond resolution (0.3 arcsec) at 144 MHz with the LOw Frequency ARray (LOFAR; van Haarlem et al. 2013). The advantage of the International LOFAR Telescope (ILT) is its wide field of view: $\sim 6 \text{ deg}^2$ from a single observation versus a few to a couple hundred arcmin² with VLBI at GHz frequencies, depending on whether one images a single phase centre or uses multiphase centres for correlation (Deller et al. 2011; Morgan et al. 2011). For example, M22 used an 8 h ILT observation of the Lockman Hole (Sweijen et al. 2022) to identify 940 AGNs via brightness temperature, providing a sample two orders of magnitude larger than any VLBI sample of AGNs identified at GHz frequencies, using a fraction of the observing time.

As part of the LOFAR Two-metre Sky Survey (LoTSS) Deep Fields campaign (Best et al. 2023, hereafter B23), we have now doubled the areal coverage of 0.3 arcsec resolution wide-field imaging. de Jong et al. (2024) recently published their 0.3 arcsec resolution image of the ELAIS-N1 field, which reaches a depth of $14 \mu\text{Jy beam}^{-1}$ using 32 h of observations. They also demonstrate the flexible resolution that can be achieved with ILT, by imaging at 0.6 and 1.2 arcsec resolution, which are both complementary to the existing 6 arcsec Deep Fields Data Release 1 (DR1; Sabater et al. 2021; Tasse et al. 2021). This is another advantage over VLBI instruments operating at GHz frequencies, which require either observing at different frequency bands or with other instruments to acquire information on the flux density of sources at other scales. As described in section 5 of M22, for sources that are unresolved in the 0.3 arcsec resolution images and do not exhibit a radio excess over that predicted by the SF rate (SFR) derived from SED fitting (see B23, for more details), we can separate the AGN activity from SF using a combination of the 0.3 and 6 arcsec resolution images.

The 2483 sources in Lockman Hole (Sweijen et al. 2022) and now the 13 058 sources in ELAIS-N1 (de Jong et al. 2024) represent a massive step towards robust statistical studies where the population can be broken into bins of redshift and stellar mass to investigate AGN and star-forming galaxy (SFG) populations in detail. Cochrane et al. (2023) and Kondapally et al. (2022) constructed radio luminosity functions (RLFs) from DR1 for the SFGs and radio-excess AGNs, respectively. Here, we construct RLFs, for the first time, by physical process rather than overall galaxy classification. We investigate the cosmic evolution of AGN activity and SF by dividing the sample into redshift bins out to $z = 2.5$.

In this letter, we first describe the data in Section 2, followed by an overview of the methods in Section 3. Section 4 describes the results, followed by conclusions in Section 5. Throughout this letter, we use an $H_0 = 70 \text{ km s}^{-1} \text{ Mpc}^{-1}$, $\Omega_M = 0.3$, and $\Omega_\Lambda = 0.7$ cosmology. Radio flux density is defined as $S \propto \nu^\alpha$, where ν is frequency and $\alpha = -0.7$ is radio spectral index.

2 DATA

2.1 LoTSS Deep Fields DR1

The LoTSS has both a wide-area (Shimwell et al. 2017, 2019, 2022) and Deep Fields (Sabater et al. 2021; Tasse et al. 2021) component.

The Deep Fields DR1 included Boötes, Lockman Hole, and ELAIS-N1, reaching sensitivities of 30, 23, and $20 \mu\text{Jy beam}^{-1}$, using ~ 80 , ~ 100 , and ~ 160 h of observations, respectively. The resolution of these images is all 6 arcsec. Alongside these deep radio images and their associated catalogues, Kondapally et al. (2021) provided a careful compilation of the ancillary data available at other wavebands [from far-infrared (FIR) to ultraviolet (UV)] and cross-matching to the radio catalogues, followed by photometric redshifts in Duncan et al. (2021). Collectively these catalogues provide an excellent resource, and we refer the reader for more details to the individual papers cited above.

Using the multiwavelength cross-matched catalogues, B23 carried out detailed SED fitting for all radio-detected sources across the three deep fields. Full details can be found in their paper, but here we outline the most relevant details. All sources detected above 5σ in their respective radio images had their FIR to UV data fit using four different SED fitting software packages, and a ‘consensus’ value was found for the derived galaxy properties using information from the goodness of fits.

The derived properties used in this letter are the consensus SFRs and the galaxy classifications, which arise from the SED fitting. B23 use the empirical relationship between radio luminosity and SFR to define sources as either *radio excess* or not. The AGN components used to fit the multiwavelength information indicate whether a source is a radiatively efficient AGN (i.e. is there evidence for a disc/torus structure) or not. Combining these provides the following classes:

- (i) Radio excess + radiatively efficient (*‘radio-loud’*)
- (ii) Radio excess + not radiatively efficient (*‘radio-loud’*)
- (iii) Radiatively efficient + not radio excess (*‘radio-quiet’*)
- (iv) Not radiatively efficient + not radio excess

The first three classes are AGNs, and the final class is SFGs. 5 per cent of all sources are unclassified, as they do not have a radio excess and the fits could not determine between radiatively efficient or inefficient. We note here that more recent work generated probabilistic classifications (Drake et al. 2024), which would have an impact on the RLFs, although the extent is a subject for future studies.

2.2 High-resolution ILT imaging

Data for LoTSS are recorded with all available ILT stations, which are spread across eight different European countries, with a preponderance of stations in the Netherlands. The longest baseline (currently Ireland to Poland) is ~ 2000 km, providing unprecedented resolution at MHz frequencies. While LoTSS uses only the stations in the Netherlands for its standard data processing, post-processing of LoTSS data to achieve sub-arcsecond resolution is ongoing both for individual sources with $S > 10 \text{ mJy}$ in the wide-area survey (Morabito et al. 2022b) and for the entire field of view in the Deep Fields (Sweijen et al. 2022; de Jong et al. 2024; Bondi et al., in preparation; Escott et al., in preparation). Due to the fact that the size of international stations is larger than that of stations in the Netherlands, the station beams have a smaller field of view. Coupled with bandwidth and time smearing, this limits the field of view effectively to a radius of 1.24 deg, which still provides 6.25 deg^2 of coverage (the imaged field of view is square with 2.5 deg per side).

Both Lockman Hole and ELAIS-N1 have been imaged at 0.3 arcsec resolution (Sweijen et al. 2022; de Jong et al. 2024, respectively). The resulting images have median rms noise of $34 \mu\text{Jy beam}^{-1}$ (Lockman Hole) and $17 \mu\text{Jy beam}^{-1}$ (ELAIS-N1), with the noise being lowest in the centre and increasing radially in both images.

Although de Jong et al. (2024) also imaged ELAIS-N1 at 0.6 and 1.2 arcsec, for consistency with Lockman Hole we use only the 0.3 arcsec resolution image. Catalogues from these images were processed to group individual Gaussian islands into complete sources, and remove duplicates. The resulting catalogues contain 2316 and 13 058 sources above 5σ , for Lockman Hole and ELAIS-N1, respectively.

Thanks to the added collecting area of the international stations, which increases the array’s sensitivity, the 0.3 arcsec resolution image for ELAIS-N1 has a lower noise level than the Deep Fields DR1. To ensure consistently built samples, and make use of DR1 information, we limit the high-resolution catalogues. For both fields, we first find the local rms in the companion 6 arcsec resolution noise maps at the position of each source in the 0.3 arcsec resolution catalogue. Using the peak brightness of the source in the catalogue from the 0.3 arcsec resolution image, we calculate the peak-to-noise ratio and only select sources that would be detectable at the 5σ limit in the 6 arcsec resolution image, effectively ensuring that all sources should have a match in DR1. We then cross-match based on radio position, to provide the radio information from the catalogues derived from both the 0.3 arcsec resolution image and the 6 arcsec resolution image. We use optical star masks to remove sources with multiwavelength information affected by bright stars. Finally, we trim the area of the multiwavelength catalogue to the $2.5 \text{ deg} \times 2.5 \text{ deg}$ area, which is covered by the 0.3 arcsec resolution image (although the multiwavelength coverage is smaller in ELAIS-N1 than in Lockman Hole). We are left with 2252 sources in Lockman Hole, and 5245 sources in ELAIS-N1.

We determine whether sources are resolved or unresolved (relevant in Section 3) in the same manner as section 3.1 of Shimwell et al. (2019, 2022), by finding an upper limit to the intrinsically unresolved sources. Theoretically, these should have equal peak brightness and total flux density, but ILT maps are impacted by smearing due to the ionosphere, and high-resolution images have time and bandwidth smearing effects. Thus, intrinsically unresolved sources can appear spatially extended. To find this upper limit, we take all sources that are fit by a single Gaussian component and are smaller than a multiple of the beam size. For the Lockman Hole, we use a factor of 3, but for ELAIS-N1 we find that a factor of 4 provided a better sample. This may be because the ELAIS-N1 field uses multiple nights, which have varying ionospheric conditions (see section 2 of de Jong et al. 2024). A sigmoid function is fit to the upper 99.9th percentile of the total flux density to peak brightness ratio as a function of local signal to noise. All sources in the catalogue that lie above this function are treated as resolved, as is any source not fitted by a single Gaussian component.

3 METHODS

Brightness temperature, T_b , is used to characterize the surface brightness of radio emission. It is not a physical temperature, but rather the temperature of a blackbody, which would produce the observed spectral radiance (assuming the Rayleigh–Jeans approximation) at long wavelengths. By creating a model that predicts the upper limit of T_b achievable by SF (based on Condon 1992), if the value is *above* that upper limit, the radio emission must be due to AGN activity. M22 showed that T_b -based AGN identification can be done at 150 MHz using sub-arcsecond resolution. We make the same conservative assumptions as M22; i.e. we set $T_e = 10^4 \text{ K}$ and the frequency where the optical depth reaches unity, ν_0 , to be 3 GHz, for the SF models. These equate to $T_b \sim 10^6 \text{ K}$ at 144 GHz (equivalent to $T_b \sim 10^5 \text{ K}$ at 1.4 GHz) as the upper limit for SF. The models directly predict flux density per solid angle, which can then be converted to

T_b values. Practically, we follow the method in M22, which simply uses a threshold in terms of flux density per solid angle rather than converting to T_b . We refer the reader to section 3 of M22 for more details. Note that this method yields conservative, positive AGN identifications.

There are two intermediate cases that may not be caught by this. For the first case, take the example of Arp 220, a late-stage merger that has been shown to have a high brightness temperature, which is consistent with an origin entirely from densely packed, very luminous radio supernovae (Smith et al. 1998; Lonsdale et al. 2006). Sub-arcsecond resolution imaging with the ILT largely supports this (Varenius et al. 2016) but cannot rule out an AGN origin for the outflow in the eastern nucleus. In this extreme case, very high SF in a compact region can mimic AGN-like values of T_b . We note that as the models of SF predict *surface brightness*, compactness of SF relative to the resolution element, which in this case is larger than for GHz VLBI, would actually *decrease* the surface brightness as the measured size would be larger than the intrinsic size. To best imitate an AGN, either the SFR has to be extreme and/or the SF has to take place in an area that is approximately the size of the beam.

The second scenario is low-surface brightness AGN emission, which mimics SF. This could be due, for example, to restarted radio AGN with a young, prominent core and low surface-brightness extended structures from previous AGN emission (e.g. Mingo et al. 2019). Or it could be due to radio emission powered by shocks from AGN winds (e.g. Zakamska & Greene 2014; Rankine et al. 2021; Petley et al. 2022). In either case, the radio emission due to SF will be overestimated, as it is contaminated by low-surface brightness AGN emission. Based on the number of new T_b identifications in M22, we expect that this is $\lesssim 10$ per cent of cases.

These two scenarios act in the opposite direction, and may balance each other out in this study. We aim to provide better constraints based on source structure (e.g. compact starbursts) and using a wider range of spatial scales in our ILT imaging (e.g. the 1.2 arcsec resolution imaging in de Jong et al. 2024) in future work.

3.1 Separation of AGN activity and SF

Once the AGN activity is identified from the 0.3 arcsec resolution images, it is possible to separate it from SF using the total flux density in the 6 arcsec resolution images. We refer the reader to section 5 of M22 for more details but outline the process here, which is depicted in Fig. 1. Sources that are identified as radio excess according to the definition in B23 (and therefore by definition have >80 per cent of flux density due to AGN) automatically have their total flux density from the 6 arcsec resolution images added to the AGN category. For sources that are not radio excess, we attribute the total flux density from the 6 arcsec resolution images to SF if in the 0.3 arcsec resolution image they either are resolved or have no detection. Sources that do not meet these criteria are checked and if their T_b is not above the limit for SF their 6 arcsec resolution total flux density is also added to the SF category. The total flux density of any source in the 0.3 arcsec resolution image that is T_b -identified as an AGN is assumed to be AGN flux density; this is subtracted from the total flux density measured from the 6 arcsec resolution image, and what remains is assumed to be flux density from SF.

In summary, we start with 7497 total sources. 2970 have a radio excess, while 4527 do not. Of those without a radio excess, there are 4434 unresolved sources for which their T_b is checked. Of those, 1022 are T_b -identified AGNs, while 3412 are not. In the final sample, there are 3992 sources contributing to the AGN category and 4527 sources contributing to the SF category. This is more than the total

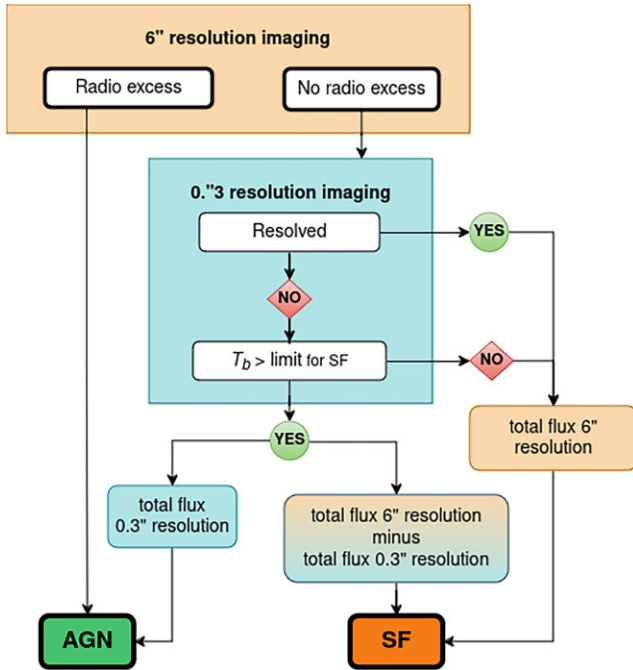


Figure 1. The workflow for determining how to assign flux density from the 6 and 0.3 arcsec resolution images to either the AGN or SF category. Only sources with a T_b -identified AGN component have their flux density split between the two categories.

number of sources due to the T_b -identified AGN, which had a portion of their flux density shifted from the SF to the AGN category.

3.2 Construction of RLFs

We follow the same method of constructing RLFs as in Kondapally et al. (2022) and Cochrane et al. (2023), which use the standard $1/V_{\max}$ method (Schmidt 1968; Condon 1989). The 0.3 arcsec resolution image is smaller than the 6 arcsec resolution image, so we first reproduce the published RLFs (Fig. 2, left panel) using the galaxy classifications from B23 to check that the RLFs in the smaller area are consistent. We use the completeness corrections from the respective papers, with the exception of the photo- z correction used in Cochrane et al. (2023). The authors note that this correction is small, and as it is not implemented in Kondapally et al. (2022) we chose to keep the method in this letter consistent across both samples. We use the same redshift range, $0.003 < z < 0.3$, to verify that we have good agreement with the published RLFs. Uncertainties are bootstrapped as in Kondapally et al. (2022), with random sampling by replacement to generate 1000 RLF realizations from which the 1σ uncertainties are determined.

Next, we use the same $1/V_{\max}$ method for constructing RLFs by physical process rather than overall galaxy classification, using the flux density of the relevant process, AGN activity, or SF, rather than the overall total flux density (where they are not the same). We directly use the completeness corrections from Cochrane et al. (2023) and Kondapally et al. (2022), based on a galaxy’s total flux density. These corrections are flux density dependent, but they are based on whether or not a source will be detectable given the background rms, not any individual component, although the component flux density can be smaller than the total flux density.

4 RESULTS

The RLFs for the physical processes of SF and AGN are shown in the middle panel of Fig. 2, for $0.003 < z < 0.3$. Comparing these with RLFs using galaxy classifications allows us to explore where we are overpredicting or underpredicting the contribution of the physical processes to our statistical studies. To aid this comparison, we define and calculate

$$\Delta\text{RLF} = \frac{\text{RLF}(\text{physical process})}{\text{RLF}(\text{galaxy classification})}$$

ΔRLF is calculated once for the SF process/SFG classification, and once for the AGN process/AGN classification. We show ΔRLF in the bottom right panel of Fig. 2. Above $10^{24} \text{ W Hz}^{-1}$, the ratio for AGN is unity, which is expected as this is where radio-excess sources dominate the population. Below that, the ratio for AGN climbs up to ~ 1.3 and finally almost up to 2 at the lowest radio powers probed. The ratio for SF is always below unity, but it does not deviate as much as the ratio for AGN. This is because the SF population has larger source counts, so the total impact of moving some flux density from the SF to AGN population is less extreme.

In Fig. 3, we show the redshift evolution for SF (left) and AGN (right). We use similar redshift bins to Kondapally et al. (2022) and Cochrane et al. (2023) for consistency. Some bins become unconstrained for the RLFs by process due to the shuffling of sources between the SF and AGN populations, yielding positive y -axis values. We remove these by cutting out bins where there is more than a 4 dex difference between the overall RLF and the process RLF. For the SF RLF, we additionally remove points > -1.8 . We reproduce previous observational results that while the SF population has a strong redshift evolution, the AGN population does not.

The bottom panels of Fig. 3 show ΔRLF , the same as in the bottom right panel of Fig. 2. For the SF population, ΔRLF is close to unity for $L_{144 \text{ MHz}} < 10^{24} \text{ W Hz}^{-1}$ in the lowest redshift bin, and then this begins to drop at higher luminosities. The higher redshift bins show similar behaviour, perhaps reaching unity at increasingly higher values of $L_{144 \text{ MHz}}$, although deeper data are needed to confirm this.

For the AGN population, ΔRLF has almost the opposite behaviour, converging to unity above $L_{144 \text{ MHz}} \sim 10^{24} \text{ W Hz}^{-1}$ for $0.003 < z < 0.3$. This is driven by the flux density of radio-excess sources, which tend to have higher radio luminosity, being entirely attributed to AGN. The convergence happens at higher luminosity for higher redshift. Below this convergence, ΔRLF increases across all redshift bins. The maximum value for each redshift bin approaches ~ 2 , although in the lowest redshift bin this stabilizes at ~ 1.3 and only climbs higher at the very lowest luminosities ($L_{144 \text{ MHz}} < 10^{22} \text{ W Hz}^{-1}$), which may be due to incompleteness.

To better quantify the integrated effect of ΔRLF , we integrate each RLF separately across the luminosity bins where the uncertainties for both RLFs are well defined, and then take the ratio of the areas. For example, for SF we integrate the RLF for the SF process and the RLF for SFGs, and divide the first by the second. These numbers are always less than unity since the SF process is overestimated in the SFG population, which has been corrected by moving T_b -identified AGN flux density contributions to the AGN process RLF. The integrated values are reported in Table 1. The mean across all redshift bins is 0.90 ± 0.02 for SF and 1.56 ± 0.06 for AGN. It is evident from the bottom right panel of Fig. 2 that this ‘hidden’ AGN population extracted from SFGs shows up in the radio AGN population at $L_{144 \text{ MHz}} < 10^{24} \text{ W Hz}^{-1}$.

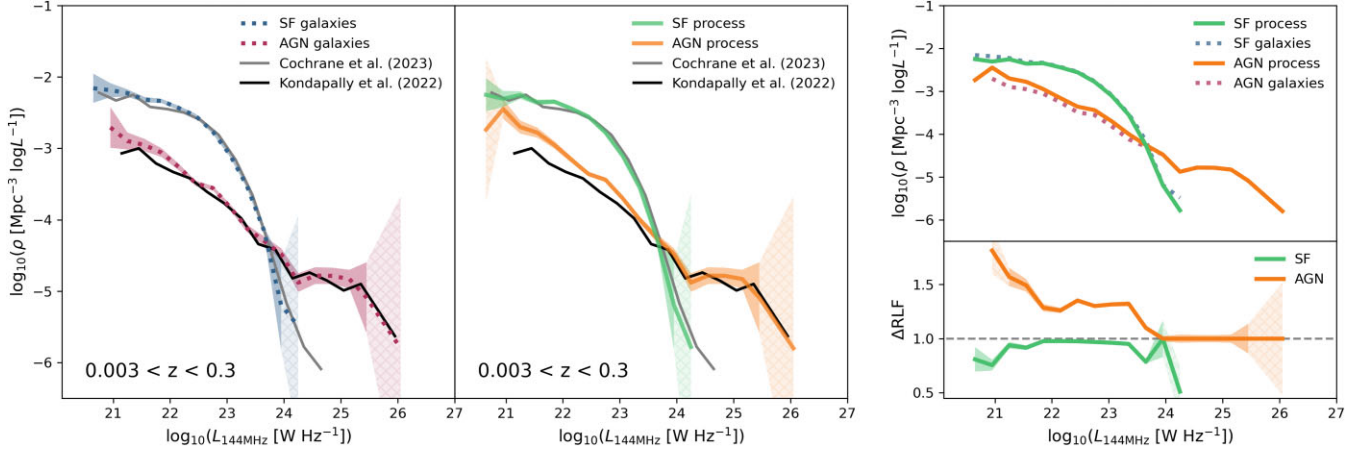


Figure 2. Left: The re-calculated galaxy RLFs (dotted lines) for the smaller area considered here, compared with previously published RLFs (solid lines). Middle: RLFs calculated by process rather than galaxy. Top right: RLFs calculated here by galaxy classifications (dotted lines) and by physical process (solid lines). Bottom right: Δ RLF for both AGN and SF. Shaded regions show the bootstrapped uncertainties, with hatched shading where the uncertainties are large and values should be treated with caution.

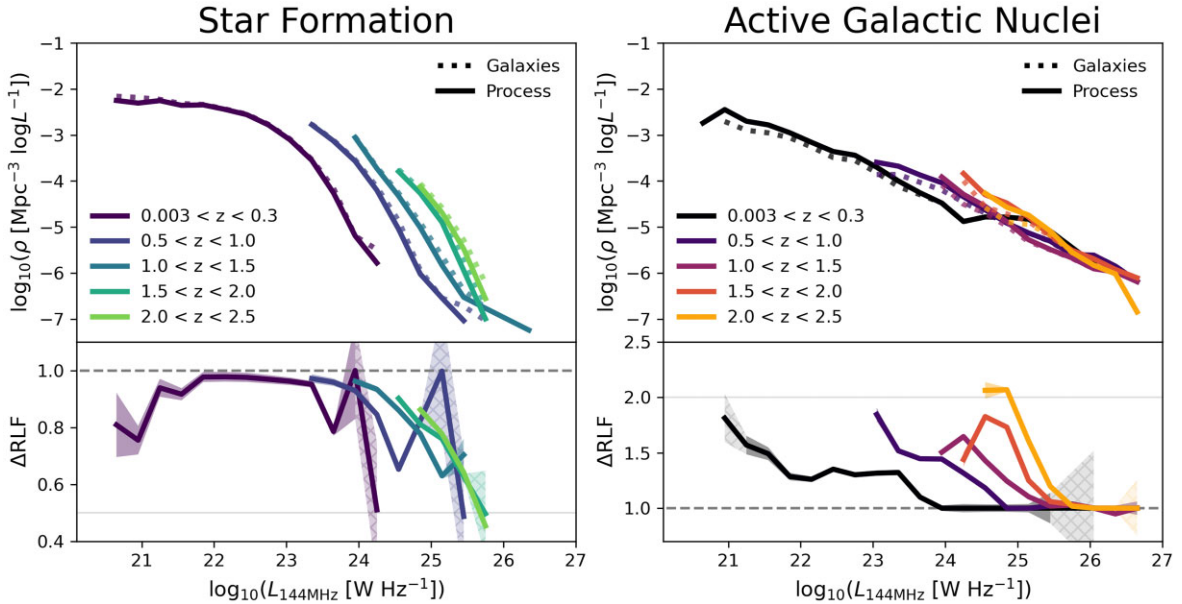


Figure 3. The redshift evolution of the RLFs (top panels) and Δ RLF (bottom panels) for SF (left) and AGN (right). The dashed horizontal line in the bottom panels is unity, with thin solid horizontal lines at 0.5 (left) at 2.0 (right) to guide the eye. To avoid overcrowding, uncertainties are only plotted for Δ RLF, in the same manner as Fig. 2.

Table 1. Integrated Δ RLF, calculated as the ratio of areas under the RLF curve by process to the RLF curve by galaxy classification.

z_{\min}	z_{\max}	SF	AGN
0.003	0.3	0.89 ± 0.12	1.52 ± 0.36
0.5	1.0	0.96 ± 0.06	1.53 ± 0.14
1.0	1.5	0.95 ± 0.07	1.47 ± 0.11
1.5	2.0	0.87 ± 0.06	1.49 ± 0.36
2.0	2.5	0.83 ± 0.06	1.80 ± 0.30

5 CONCLUSIONS

In this letter, we presented, for the first time, RLFs constructed by separating radio emission into either SF or AGN processes, for 7497 sources. We use brightness temperature to identify AGN components

in galaxies with no radio excess, and separate the radio emission into AGN and SF. We compare these with classical RLFs constructed using galaxy classifications, and find a hidden AGN population in sources with $L_{144 \text{ MHz}} \lesssim 10^{24} \text{ W Hz}^{-1}$. The mean integrated impact of this is a 1.52 ± 0.06 increase in the radio luminosity output due to AGN across intermediate redshifts ($0.5 < z < 2.0$), and a doubling in the lowest redshift bin ($0.003 < z < 0.3$). The impact on the SFG population is less severe, amounting to a mean integrated decrease in the RLF to 0.90 ± 0.02 . The results can have implications for the cosmic SFR density and kinetic luminosity density, which we will explore in a future paper.

This study is only now possible thanks to the ILT's exceptional combination of resolution and field of view. The sub-arcsecond resolution is sufficient for brightness temperature identification of AGN, and the field of view means that we have been able to

this for 1022 sources (out of >4000). We have used conservative limits for AGN identification, which means that there is likely more AGN emission still remaining ‘uncounted’. Future work will build a forward modelling method, which will also use intermediate-resolution images to improve the AGN and SF separation. Splitting radio emission into category by physical process also opens a pathway for direct comparison to cosmological simulations, which we will address in a future paper.

ACKNOWLEDGEMENTS

LKM recognizes support from UK Research and Innovation (UKRI; grantMR/T042842/1). RK recognizes support from UK Science and Technology Facilities Council (STFC) via grant ST/V000594/1. PNB recognizes support from UK STFC via grants ST/V000594/1 and ST/Y000951/1. B-HY thanks the University of Edinburgh and Leiden Observatory for support through the Edinburgh–Leiden joint studentship. JMGHJ recognizes support from project CORTEX (NWA.1160.18.316) of research programme NWA-ORC, which is (partly) financed by the Dutch Research Council (NWO). FS recognizes support from STFC (ST/Y004159/1). MB and IP recognize support from Istituto Nazionale di Astrofisica (INAF) under the Large Grant 2022 funding scheme (project ‘MeerKAT and LOFAR Team up: a Unique Radio Window on Galaxy/AGN co-Evolution’). DJBS recognizes support from UK STFC via grants ST/V000624/1 and ST/Y001028/1. RJvW recognizes support from European Research Council (ERC) Starting Grant ClusterWeb 804208. This work was supported by SURF Cooperative grant EINF-6218 and EGI-ACE project (Horizon 2020 grant 101017567).

The LOFAR was designed and constructed by ASTRON. It has observing, data processing, and data storage facilities in several countries, which are owned by various parties (each with their own funding sources), and collectively operated by the ILT foundation under a joint scientific policy. The ILT resources have benefited from the following recent major funding sources: CNRS-INSU, Observatoire de Paris and Université d’Orléans, France; BMBF, MIWF-NRW, MPG, Germany; Science Foundation Ireland (SFI), Department of Business, Enterprise and Innovation (DBEI), Ireland; NWO, the Netherlands; The Science and Technology Facilities Council, UK; Ministry of Science and Higher Education, Poland; and The INAF, Italy.

DATA AVAILABILITY

All data used in this letter are either publicly available on <https://lofar-surveys.org> or from relevant citations herein, including catalogues, rms images, and star masks. This study was carried out using showyourwork (<https://github.com/showyourwork/showyourwork>), which is open source scientific article workflow, first introduced in Luger et al. (2021). This leverages continuous integration to programmatically download the data from zenodo.org, create the figures, and compile the manuscript. The code is available at https://github.com/Imorabit/hidden_AGN, which is linked to the starting data sets for this work, which are hosted on Zenodo with their own DOIs

(10.5281/zenodo.14012620, 10.5281/zenodo.14013377, 14013423, 14013439, 14014490, 14014542, 14014849, and 14014853), ensuring complete reproducibility.

REFERENCES

- Best P. N. et al., 2023, *MNRAS*, 523, 1729(B23)
 Boquien M., Burgarella D., Roehilly Y., Buat V., Ciesla L., Corre D., Inoue A. K., Salas H., 2019, *A&A*, 622, A103
 Bower R. G., Benson A. J., Malbon R., Helly J. C., Frenk C. S., Baugh C. M., Cole S., Lacey C. G., 2006, *MNRAS*, 370, 645
 Calistro Rivera G., Lusso E., Hennawi J. F., Hogg D. W., 2016, *ApJ*, 833, 98
 Cochrane R. K. et al., 2023, *MNRAS*, 523, 6082
 Condon J. J., 1989, *ApJ*, 338, 13
 Condon J. J., 1992, *ARA&A*, 30, 575
 Croton D. J. et al., 2006, *MNRAS*, 365, 11
 de Jong J. M. G. H. J. et al., 2024, *A&A*, 689, A80
 Deller A. T. et al., 2011, *PASP*, 123, 275
 Drake A. B. et al., 2024, *MNRAS*, 534, 1107
 Duncan K. J. et al., 2021, *A&A*, 648, A4
 Hernán-Caballero A. et al., 2015, *ApJ*, 803, 109
 Herrera Ruiz N. et al., 2017, *A&A*, 607, A132
 Kondapally R. et al., 2021, *A&A*, 648, A3
 Kondapally R. et al., 2022, *MNRAS*, 513, 3742
 Kormendy J., Ho L. C., 2013, *ARA&A*, 51, 511
 Laurent O., Mirabel I. F., Charmandaris V., Gallais P., Madden S. C., Sauvage M., Vigroux L., Cesarsky C., 2000, *A&A*, 359, 887
 Li Z.-J., Dai Y. S., Huang J. S., Wuyts S., Cao T.-W., 2024, *ApJ*, 963, 99
 Lonsdale C. J., Diamond P. J., Thrall H., Smith H. E., Lonsdale C. J., 2006, *ApJ*, 647, 185
 Luger R., Bedell M., Foreman-Mackey D., Crossfield I. J. M., Zhao L. L., Hogg D. W., 2021, preprint ([arXiv:2110.06271](https://arxiv.org/abs/2110.06271))
 Middelberg E. et al., 2013, *A&A*, 551, A97
 Mingo B. et al., 2019, *MNRAS*, 488, 2701
 Morabito L. K. et al., 2022a, *MNRAS*, 515, 5758(M22)
 Morabito L. K. et al., 2022b, *A&A*, 658, A1
 Morgan J. S., Mantovani F., Deller A. T., Brisken W., Alef W., Middelberg E., Nanni M., Tingay S. J., 2011, *A&A*, 526, A140
 Pacifici C. et al., 2023, *ApJ*, 944, 141
 Petley J. W. et al., 2022, *MNRAS*, 515, 5159
 Radcliffe J. F. et al., 2018, *A&A*, 619, A48
 Rankine A. L., Matthews J. H., Hewett P. C., Banerji M., Morabito L. K., Richards G. T., 2021, *MNRAS*, 502, 4154
 Sabater J. et al., 2021, *A&A*, 648, A2
 Schmidt M., 1968, *ApJ*, 151, 393
 Shimwell T. W. et al., 2017, *A&A*, 598, A104
 Shimwell T. W. et al., 2019, *A&A*, 622, A1
 Shimwell T. W. et al., 2022, *A&A*, 659, A1
 Smith H. E., Lonsdale C. J., Lonsdale C. J., Diamond P. J., 1998, *ApJ*, 493, L17
 Sweijen F. et al., 2022, *Nat. Astron.*, 6, 350
 Tasse C. et al., 2021, *A&A*, 648, A1
 van Haarlem M. P. et al., 2013, *A&A*, 556, A2
 Varenus E. et al., 2016, *A&A*, 593, A86
 Zakamska N. L., Greene J. E., 2014, *MNRAS*, 442, 784

This paper has been typeset from a $\text{\TeX}/\text{\LaTeX}$ file prepared by the author.